






# Temperature-driven transition into vortex clusters in low-kappa intertype superconductors

A. Backs <sup>1,2,\*</sup>, A. Al-Falou <sup>3,4</sup>, A. Vagov <sup>5</sup>, P. Böni <sup>4</sup>, and S. Mühlbauer <sup>3,†</sup>

<sup>1</sup>*Department of Mechanical Engineering Sciences, Lund University, 221 00 Lund, Sweden*

<sup>2</sup>*European Spallation Source ERIC, 224 84 Lund, Sweden*

<sup>3</sup>*Heinz Maier-Leibnitz Zentrum (MLZ), Technische Universität München, 85748 Garching, Germany*

<sup>4</sup>*Physik-Department E21, Technische Universität München, 85748 Garching, Germany*

<sup>5</sup>*Institut of Theoretical Physics Physics III, University of Bayreuth, 95440 Bayreuth, Germany*



(Received 16 January 2023; revised 18 April 2023; accepted 20 April 2023; published 31 May 2023)

In the vicinity of the type-I/type-II crossover in conventional superconductors, vortices exhibit a nonmonotonic interaction, which leads to exotic vortex matter states. We perform molecular dynamics simulations on a model superconductor in the intertype regime. In a field cooled approach, we examine the transition of a homogeneous vortex lattice (VL) into a structure consisting of VL domains and Meissner-state domains. The results show extraordinary stability of the transition against vortex pinning and a strong dependence on the external magnetic field.

DOI: [10.1103/PhysRevB.107.174527](https://doi.org/10.1103/PhysRevB.107.174527)

## I. INTRODUCTION

Conventionally, vortex interactions are assumed to be either attractive or repulsive, which directly corresponds to the distinction between type-I and type-II superconductors [1]. However, a nonmonotonic interaction is possible, which results in exotic vortex structures and has attained increased interest in recent years. Historically, the effects of such interactions were first observed in conventional superconductors with Ginzburg-Landau parameter  $\kappa \simeq \kappa_0 = 1/\sqrt{2}$ , referred to as low-kappa type-II/1 materials [2]. Here the intermediate mixed state (IMS) is observed with a domain structure in the vortex matter, consisting of vortex lattice (VL) and flux-free Meissner state [3]. The origin of the nonmonotonic interaction is explained with an energetically beneficial partial overlap of the vortex cores, due to very similar length scales defined by the magnetic penetration depth  $\lambda_L$  and the coherence length  $\xi_{GL}$  in the vicinity of  $\kappa_0$ , sometimes referred to as the Bogomolny critical point [4].

Subsequently, similarities to the IMS behavior have been found in other superconductors, e.g.,  $ZrB_{12}$ ,  $LuB_{12}$  [5–7], and  $MgB_2$  [8], which rekindled the interest for this phenomenon [9].  $MgB_2$  poses an especially interesting case, where two electronic bands contributing to the superconducting state, each with distinct  $\lambda_L$  and  $\xi_{GL}$  [10,11]. It was argued that when one of the bands corresponds to a classical type-I superconductor and the other one has characteristics of a type-II

superconductor, the total system is classified as a type-1.5 superconductor with the vortex interaction being attractive at large and repulsive at small distances [7,8,12]. The nonmonotonic interaction has also been observed in superconducting thin films and layered materials, where the stray field and anisotropy due to field canting play a pivotal role [13–15]. A domain structure similar to the IMS has also been found in the spin triplet superconductor  $Sr_2RuO_4$  [16].

The interest in the type-II/1 behavior and IMS was renewed by recent theoretical advances in the investigation of low- $\kappa$  ( $\kappa \simeq \kappa_0$ ) type-II superconductors. A recent analysis, based on the extended Ginzburg-Landau (EGL) approach, described details of a transition to the regime of nonmonotonic vortex interaction [17,18], confirming earlier numerical microscopic BCS theory calculations [4]. Additionally, an increasing importance of multivortex interactions was demonstrated in stabilizing large vortex clusters even if the pairwise vortex interaction becomes fully attractive [19]. The nonmonotonic and multivortex interactions take place in a transitional domain between the classical type-I and type-II regimes. It exceeds the earlier discussed type-II/1 superconductivity domain, and is labeled as intertype (IT) superconductivity. The IT domain encompasses the IMS, as well as other exotic vortex matter states, such as multiquantum vortices and liquid multivortex droplets [18].

It turned out that EGL results for IT superconductivity in conventional single-band BCS superconductors [17,18] are very similar qualitatively to two-band superconductors described within a model of two linearly coupled GL equations [12,20,21], including vortex interactions, IMS configurations, and the overall topological structure of the IT domain. Notably, most of the results for the IMS in two-band superconductors can be reproduced using the EGL formalism [17], although, the full range of applicability of perturbative approaches to the BCS theory is currently a subject of discussions [22].

\*alexander.backs@material.lth.se

†sebastian.muehlbauer@frm2.tum.de

To summarize the current state of the art, the key requirement for the IMS is a nonmonotonic vortex interaction, where the competition between repulsion and attraction gives rise to vortex clusters and domain structures. Such interactions are of sufficiently general nature that they can be reproduced within different levels of approximation, including direct solutions to microscopic models. Nonmonotonic interactions with more than one characteristic length scale unite IT superconductors with a very wide class of systems with spontaneously emerging complex patterns. It is known that fine details of the interaction potential, e.g., its asymptotic behavior, are of secondary importance for the pattern formation. Therefore, it is not surprising that one observes qualitatively similar IMS vortex configurations in various superconducting materials.

Despite recent progress, understanding the phenomenon of IT superconductivity is far from being comprehensive. Research is hampered by the lack of adequate theoretical and experimental tools. Experimental techniques capable of resolving individual vortices, such as scanning tunneling microscopy [23], magnetic force microscopy [24], and magneto-optical imaging [25], are restricted to probing surfaces and thin films. On the other hand, bulk sensitive methods like neutron scattering [26] or muon spin rotation [7], cannot map the microscopic vortex patterns. Further advances in the theory require adequate methods that can describe the highly inhomogeneous IMS with a large number of vortices, while taking into account other factors like anisotropy and disorder. In this regard, numerical simulations, especially of the molecular dynamics kind, offer a powerful tool to investigate the IMS and offer results, necessary to understand IMS physics and to interpret experimental data.

In this paper, we employ molecular dynamics simulations to investigate the dependence of the IMS on the magnetic field and pinning potential in large systems of many vortices. The study is motivated by our recent experiments on bulk niobium [27–29] that investigated the transition between the classical type-II VL and the IMS, obtained by field cooling under the condition of nearly perfect macroscopic flux trapping. The most prominent hallmark of the IMS is the separation of neighboring vortices, which has a characteristic temperature dependence but is independent of the field. Additionally, the experiments revealed a temperature-independent characteristic length scale of the emerging vortex superstructures.

In our study, vortices are regarded as interacting “particles”. Their configurations are found using molecular dynamics methods [30–35]. For the simulations we adopt a realistic model for the inter-vortex potential extracted from earlier theoretical calculations for two vortices. The pinning potential is modeled by introducing static point defects with a short range attraction. The calculations reveal that the IMS is exceptionally robust with respect to pinning. However, vortex pinning affects the field dependence of the IMS transition, and its characteristic length scales.

The paper is organized as follows. In the Methods (Sec. II), the simulation algorithm is described, including details of the EGL vortex-vortex interaction. The Numerical Results (Sec. III) is headed by a description of the data analysis, followed by an assessment of pinning free simulations

(Sec. III A) concerning their physical relevance, especially with respect to the cooling procedure. Afterwards, we present our results on the interplay between pinning and the IMS transition (Sec. III B), and finally the impact of the external magnetic field (Sec. III C). For the latter, we first perform an extensive study on the role of the two relevant pinning parameters for a fixed magnetic field, and afterwards address the field dependence of the IMS in three qualitatively distinct pinning regimes.

## II. METHOD

### A. Molecular dynamics

To investigate the IMS vortex matter we employ a two-dimensional molecular dynamics (MD) approach [36], where vortices are treated as elementary “particles” of the mixed state. This is a reasonable approximation when dealing with a large number of vortices with pairwise interactions. Many-body contributions to the vortex interactions only become important close to the type-I regime [19], which is not the case in this study. The simulations have a reduced dimensionality, working in the 2D plane perpendicular to the direction of the magnetic field and vortex lines. This is a commonly used approach to reduce the amount of time full-3D simulations require and therefore enable larger vortex matter systems and an extended range of simulation parameters. We justify this simplification by referring to our previous experiments, which are the bases of this paper and which are to be emulated as closely as possible. In the first study, results from neutron scattering showed a correlation length of vortices in the IMS of above 10  $\mu\text{m}$  along the field [29,37]. In a second study, even under the effect of a driving current vortices were found to bend less than a few degrees [38]. Both results justify the simplification to locally treat vortices as straight, rigid lines in the scope of this paper and use two-dimensional simulations without losing physical relevance of the results.

The MD method is based on the Langevin-type equations that simulate the highly dissipative vortex dynamics [39–42]

$$r_i(t + \Delta t) = r_i(t) + v_i(t) \Delta t + \delta r_{\text{th},i}(t),$$

$$v_i(t) = \frac{F_i(t)}{\eta} + \exp\left(-\frac{1}{\gamma}\right) v_i(t - \Delta t), \quad (1)$$

where  $r_i$  and  $v_i$  are, respectively, the position and velocity of an  $i$ th vortex, on which the force  $F_i$  is acting, comprising the intervortex force  $F_{\text{vv}}$  and the vortex-pinning force  $F_{\text{vp}}$ . A further contribution to the vortex dynamics is provided by thermally induced fluctuations, modeled here by random jumps  $\delta r_{\text{th},i}$ . The duration of a simulation step  $\Delta t$  is not constant in our approach and is changed dynamically to achieve better accuracy and convergence (see Appendix A for detailed description). The Bardeen-Stephen friction coefficient [43]

$$\eta = \frac{\phi_0^2}{2\pi \xi_{\text{GL},0}^2 \rho_{\text{res}}} \quad (2)$$

is determined by the zero temperature Ginzburg-Landau correlation length  $\xi_{\text{GL},0}$ , the residual resistivity  $\rho_{\text{res}}$  of the normal conducting state, and the magnetic flux quantum  $\phi_0$ . Finally,

TABLE I. Parameters defining the superconducting model system used in the calculations. The values were chosen to resemble the single crystal niobium sample MP-1 in [29], where  $\lambda_0$  and  $\xi_0$  are the magnetic penetration and coherence lengths at  $T = 0$ .

$T_c$	$\lambda_0$	$\xi_0$	$\delta\kappa$	$B_{c2,0}$	$\rho_{res}$
9.2 K	32 nm	39.7 nm	0.1	450 mT	$3 \times 10^{-10} \Omega\text{m}$

we optimize the simulation convergence by including an exponential relaxation of the vortex velocities with the relaxation constant  $\gamma$ . The limit  $\gamma \rightarrow 0$  restores the overdamped Langevin equation.

### B. Model superconductor

For the simulations we use material parameters resembling superconducting Nb, which are given in Table I. Both the magnetic penetration length and the coherence length diverge as  $\lambda_L, \xi_{GL} \propto \tau^{-1/2}$ , in the vicinity of the critical temperature  $T_c$ , with  $\tau = 1 - T/T_c$ . Accordingly, the GL parameter  $\kappa = \lambda_L/\xi_{GL}$  is temperature independent. All three characteristic parameters are independent of the magnetic field. For Nb,  $\delta\kappa = \kappa - \kappa_0 \simeq 0.1$ , which places it in the class of low-kappa type-II superconductors in classical GL theory. According to the analysis of the IT domain in single-band superconductors, Nb is a type-II material close to  $T_c$  and crosses over into the IT regime at lower temperatures.

### C. Vortex-vortex interaction

The vortex-vortex interaction  $F_{vv}$  is a function of the vortex separation  $r$  and is modeled using the results of calculations for clean, single-band superconductor with isotropic gap within the EGL formalism as a function of the vortex separation  $r$  [17]. Vortex interactions have a pairwise character in the considered temperature range, while multivortex contributions are significant only at very low temperatures. Figure 1(a) illustrates its temperature dependence. At  $T = 9\text{K} \simeq T_c$  the system is in the type-II regime, where vortices are repulsive and  $F_{vv} > 0$ . Notably, the force  $F_{vv}$  approaches zero not only in the limit of large distance, but also in the limit of small ones.

At lower temperatures, the material crosses over into the IT domain, where the intervortex force becomes attractive at larger distances while remaining repulsive at smaller ones. This nonmonotonic behavior is the key feature of the IMS in the IT domain. The interaction features a potential minimum, with zero force  $F_{vv} = 0$ , whose position at  $r_{vv}^{\min}$  decreases with decreasing  $T$ . Hence, the average distance between vortices in the IMS state becomes smaller, which corresponds to an increasing average magnetic flux density in the emerging vortex clusters. The temperature dependence of  $r_{vv}^{\min}$  is shown in Fig. 1(b) by the blue line. In an extended lattice, the overall energy is minimal at the distance  $r_{VL}^{\min}$  between neighboring vortices, which slightly differs from the pair wise potential due to the numerous contributions of subsequent neighbours. The effect has been calculated for a hexagonal VL and is included as the orange line in the same figure. Both values are close and increase monotonically with the rising

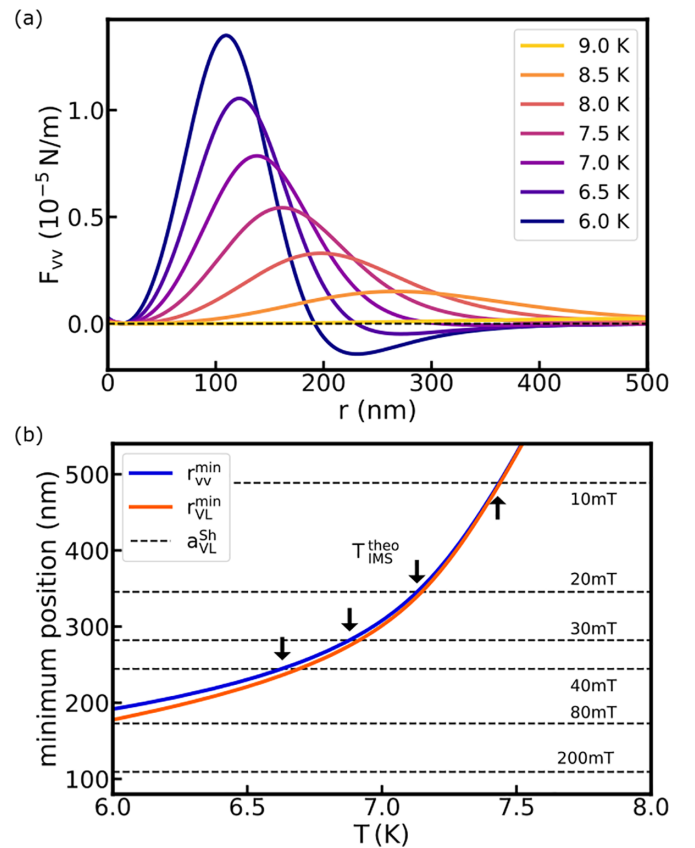


FIG. 1. (a) Vortex-vortex force  $F_{vv}(r)$  at selected temperatures in the range relevant for this paper. Positive values correspond to vortex repulsion and negative values to attraction. (b) Temperature dependence of the interaction potential minimum, which defines the optimal vortex separation.  $r_{vv}^{\min}$  (blue) corresponds to the case of two vortices, while  $r_{VL}^{\min}$  (orange) depicts the optimal VL parameter in a hexagonal lattice.  $a_{VL}^{\text{Sh}}$  (black) shows the lattice parameter of a hexagonal VL with the indicated flux density. The intersection of  $r_{VL}^{\min}$  with the constant lattice parameter  $a_{VL}^{\text{Sh}}$  defines the theoretical IMS transition temperature  $T_{\text{IMS}}^{\text{theo}}$ .

temperature. Finally, the figure plots the vortex separation in hexagonal Abrikosov lattices corresponding to the specified average magnetic field, shown by the grey dashed lines.

Notice that our analysis is restricted to the temperature interval of  $0.7T_c \lesssim T \lesssim T_c$ , where the EGL approach is applicable. At lower temperatures, one needs to retain higher order corrections in the  $\tau$  expansion of the pertinent quantities. In this interval, pairs of vortices can become fully attractive, but larger vortex clusters are stabilized by multivortex interactions. A detailed analysis of this low temperature regime is, however, beyond the scope of this paper.

### D. Pinning potential

Vortex pinning is included by adopting a conventional model of randomly distributed point defects with a short-range attractive Gaussian potential due to the pinning site overlapping with the vortex core [31–33,44,45]. The interactions decreases the overall energy gain associated with the

superconducting state. The pinning force writes as

$$F_{pv}(r) = v_p \frac{\pi}{2\mu_0\kappa^2} B_{c2}^2 \left(1 - \frac{B}{B_{c2}}\right) r e^{-r^2/\xi_{GL}^2} \quad (3)$$

where the factor  $0 \leq v_p \leq 1$  determines how effective the pinning potential suppresses superconductivity. For the temperature dependence of the upper critical magnetic field we use the Gorter-Casimir expression  $B_{c2} \propto B_{c2,0}(2\tau - \tau^2)$ . However, in the temperature range of  $T \gtrsim 0.7T_c$ , only the linear contribution is important.

### E. Thermal fluctuations

Since the IMS is a feature observed in bulk superconductors, we assume random displacements of the vortex positions  $\delta r_{th}$  to model thermal fluctuations, instead of the statistical thermal force commonly used for simulations of thin films [46–48]. Random jumps  $\delta r_{th}$  obey a Gaussian distribution with the standard deviation given by linear elasticity theory [49–51] as

$$\sigma_{th} = \frac{\mu_0 \lambda_L \kappa k_B T}{\phi_0 B} \sqrt{\frac{2b}{(1-b)^3}} \quad (4)$$

where  $k_B$  is the Boltzmann constant and  $b = B/B_{c2}(T)$  is the reduced flux density.

## III. NUMERICAL RESULTS

Using the MD equations (1) we have performed simulations at various parameters in order to clarify their role in the formation of IMS vortex patterns. With reference to previous experiments, we adopt a field-cooling protocol in the presence of perfect macroscopic flux trapping [29]. Experimentally, it was observed that the sample magnetization remains zero in the superconducting state, meaning that vortices are unable to leave the sample. To represent this, we keep the number of vortices  $N_v$  and the sample area  $A$  constant in each simulation. The number of pinning sites  $N_p$  is fixed as well and they are assumed to be distributed randomly.

The simulations are done using the following sequence of steps. Vortices are initially arranged in a hexagonal lattice. The field-cooling protocol implies the simulations are started at higher temperature  $T_i$  and the equilibrium vortex configuration is obtained using  $S_T$  steps in the Langevin equations (1). The temperature is then decreased by a given increment  $\Delta T$ , and a new vortex configuration is found starting from the one obtained in the previous step. The procedure is repeated until we reach the final temperature  $T_f$ . Effectively,  $\Delta T$  amounts to a quench of the system, while  $S_T$  controls the ability to relax into the new state. The applied magnetic field defines the vortex density  $\rho_v = N_v/A = B/\phi_0$ . In order to seamlessly fit a hexagonal lattice into the simulation cell, we consider a rectangular sample with an aspect ratio of  $2 : \sqrt{3}$  and use periodic boundary conditions.

A typical example of the vortex structure obtained after field cooling into the IMS is shown in Fig. 2(a). It consists of regions containing an ordered vortex lattice, and vortex-free domains in the Meissner state. For quantitative evaluation and to compare results of the simulations with the neutron

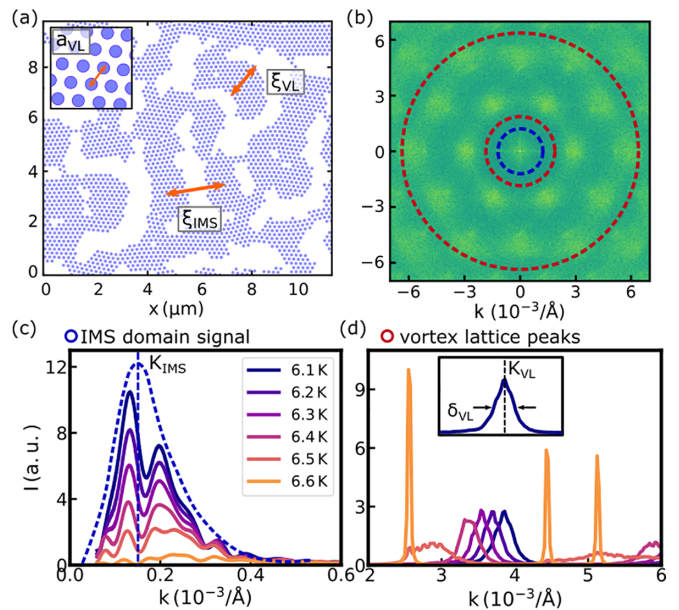


FIG. 2. (a) Real space image of the vortex positions after field cooling into the IMS. (b) Fourier transform of the vortex distribution, including signals from the vortex lattice (between red circles) and the IMS domains (inside blue circle). (c) Radial average of the Fourier transform at several temperatures in the low- $k$  region, showing the emerging IMS domain signal. The signal from the initial simulation step has been subtracted as a background. (d) High- $k$  region of the radial average, containing the VL signal. In the IMS, the VL-peaks are shifting and significantly broadened.

scattering experiments we calculate the Fourier transform of the obtained configurations as shown in Fig. 2(b). The hexagonal structure clearly visible between red dashed circles is a manifestation of the hexagonal VL inside the vortex domains in Fig. 2(a). Positions of the peaks in the reciprocal space yield the VL lattice parameter  $a_{VL} = 4\pi K_{VL}/\sqrt{3}$ , where  $K_{VL}$  is the distance between  $k = 0$  and the closest peak at  $k \neq 0$ . Irregular vortex domains of various shape and size give rise to the central peak at  $k = 0$  inside the blue dashed circle in Fig. 2(b).

For the quantitative analysis of IMS structures, we calculate angular averages of the Fourier transform in the reciprocal space. The intensity peaks found in the averages correspond to the characteristic length scales of the vortex matter. In Fig. 2(c) the signature of the IMS domains is found in the low range  $k < 0.6 \times 10^{-3} \text{ \AA}^{-1}$ . The center position of the peak  $K_{IMS}$  gives an estimate of the length scale defining the domain structure  $\xi_{IMS} = 2\pi/k_{IMS}$ . Figure 2(d) shows the interval at larger  $k < 6 \times 10^{-3} \text{ \AA}^{-1}$  that corresponds to the length scale of the VL inside the domains. The peaks corresponding to the hexagonal lattice are clearly visible. Using their width  $\delta k$ , the average VL domain size is estimated as  $\xi_{VL} = 2\pi/\delta k$ .  $\xi_{IMS}$  and  $\xi_{VL}$  are also indicated exemplarily in Fig. 2(a). Note, that the determination of the VL properties  $K_{VL}$  and  $\xi_{VL}$  is very precise and reliable, while the position of the IMS peak  $K_{IMS}$  is less well defined due to the large size of domains compared to the simulation area and finite size effects of the limited simulation area.



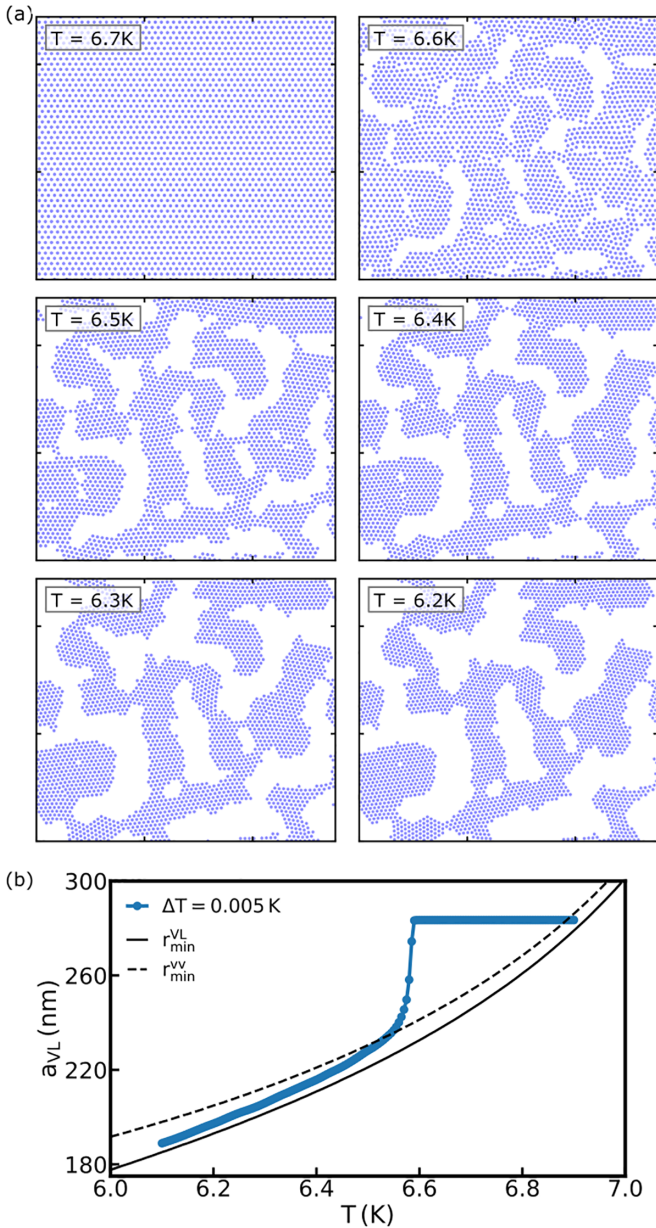


FIG. 3. (a) Real space images of a pinning free exemplary simulation at temperatures close to the IMS transition. (b) Temperature dependence of the VL parameter  $a_{\text{VL}}(T)$ . The initial constant vortex separation shows the type-II character of the superconductor at higher temperatures. Below a critical temperature  $T_{\text{I}t\text{e}l\text{I}M\text{S}}$ ,  $a_{\text{VL}}(T)$  decreases and follows the predicted IT behavior.

### A. Clean system

The IMS formation mechanism can be most easily traced using a clean system without impurities. Figure 3(a) shows results of the simulations performed at selected temperatures close to the IMS transition. At high temperatures, the vortices are repulsive and the initial hexagonal VL remains stable. When the temperature is lowered the VL breaks into domains of random size and shape.

The transition from the Shubnikov mixed state into the IMS can be characterized using the average distance between neighboring vortices  $a_{\text{VL}}$  in the system as a transition

parameter. It is plotted in Fig. 3(b) as a function of temperature  $T$  together with positions of the interaction energy minima,  $r_{\text{VV}}^{\text{min}}$  and  $r_{\text{VL}}^{\text{min}}$ , for comparison. When the temperature decreases, the intervortex distance remains constant initially. Then one observes a sharp drop in  $a_{\text{VL}}$  at  $T \simeq 6.6\text{ K}$ , indicating a first order phase transition. With the further decrease of  $T$ , the distance  $a_{\text{VL}}$  follows essentially the temperature dependence of the minimum potential position  $r_{\text{min}}$ . The curve shows the common feature of an undercooling below the expected transition temperature  $T_{\text{IMS}}^{\text{theo}}$ .

The transition is driven by the changing vortex interaction with decreasing  $T$  (see Fig. 1). Close to the critical temperature  $T \rightarrow T_c$  the purely repulsive interaction creates a VL, where the vortex separation is determined by the global flux density, which is independent of  $T$ . At lower temperature, the interaction becomes nonmonotonic, with a decreasing equilibrium position  $r_{\text{min}}$ . When  $r_{\text{min}}$  falls below the average vortex separation, the VL becomes unstable against the formation of clusters. However, it remains locally stable, creating an undercooled state with a metastable VL. Only below a critical temperature  $T_{\text{IMS}}$  the VL breaks apart and the IMS vortex clusters form. Inside the clusters vortices still form a hexagonal VL, however, their separation is now determined by the interaction potential, with  $a_{\text{VL}} \simeq \tilde{r}_{\text{min}}$ .

To test the convergence of the calculations we take different increment values  $\Delta T = 0.005, 0.01, 0.02, 0.05, 0.1\text{ K}$ , while  $S_T$  is chosen such that an average “cooling rate” is constant  $S_T/\Delta T = 5000$  steps/K. The calculations reveal that the approach is insensitive to this choice and the final IMS domain morphology at  $T_{\text{fin}} = 6.1\text{ K}$  is practically indistinguishable (see Appendix B; Fig. 7 shows the final vortex configurations for all values of  $\Delta T$  and the evolution of  $a_{\text{VL}}$ ).

The number of simulation steps  $S_T$  and the relaxation parameter  $\gamma$  control the relaxation process of the vortex matter after each temperature jump  $\Delta T$ . We have performed simulations for all combinations of  $\gamma = 0, 1, 2, 4, 8, 16$  and  $S_T = 6, 13, 25, 50, 100$  to examine the effect of both parameters. Images of the resulting vortex configurations and numerical results are shown in Fig. 8 and in Appendix B. Increasing  $\gamma$  and  $S_T$  leads to an increase of the domain size without a significant change of the morphology. This is visually obvious and confirmed by numerical results of the correlation lengths  $\xi_{\text{VL}}$ ,  $\xi_{\text{IMS}}$ , and the total vortex interaction energy  $E_{\text{tot}}$ . The domain size varies by a factor of about 4 in the evaluated parameter space. For high  $S_T$  and  $\gamma$ , it exceeds  $\xi_{\text{IMS}} > 6\text{ }\mu\text{m}$ , which is comparable to the simulation area and therefore regarded as unreliable. The IMS transition temperature  $T_{\text{IMS}}$  only changes slightly, by approximately 0.08 K, which is much less than the undercooling of 0.3 – 0.4 K.

The pinning free simulations have shown the importance of undercooling the lattice below the predicted transition temperature. This introduces a substantial quenching of the VL parameter  $a_{\text{VL}}$  at the IMS transition. We attribute the undercooling to the perfect arrangement of the initial VL, which creates a metastable state. This is also reflected in the weak dependence of  $T_{\text{IMS}}$  on the parameters  $\gamma$  and  $S_T$ .

For all following simulations, we use the parameters  $\Delta T = 0.01\text{ K}$ ,  $\gamma = 4$ , and  $S_T = 25$ .

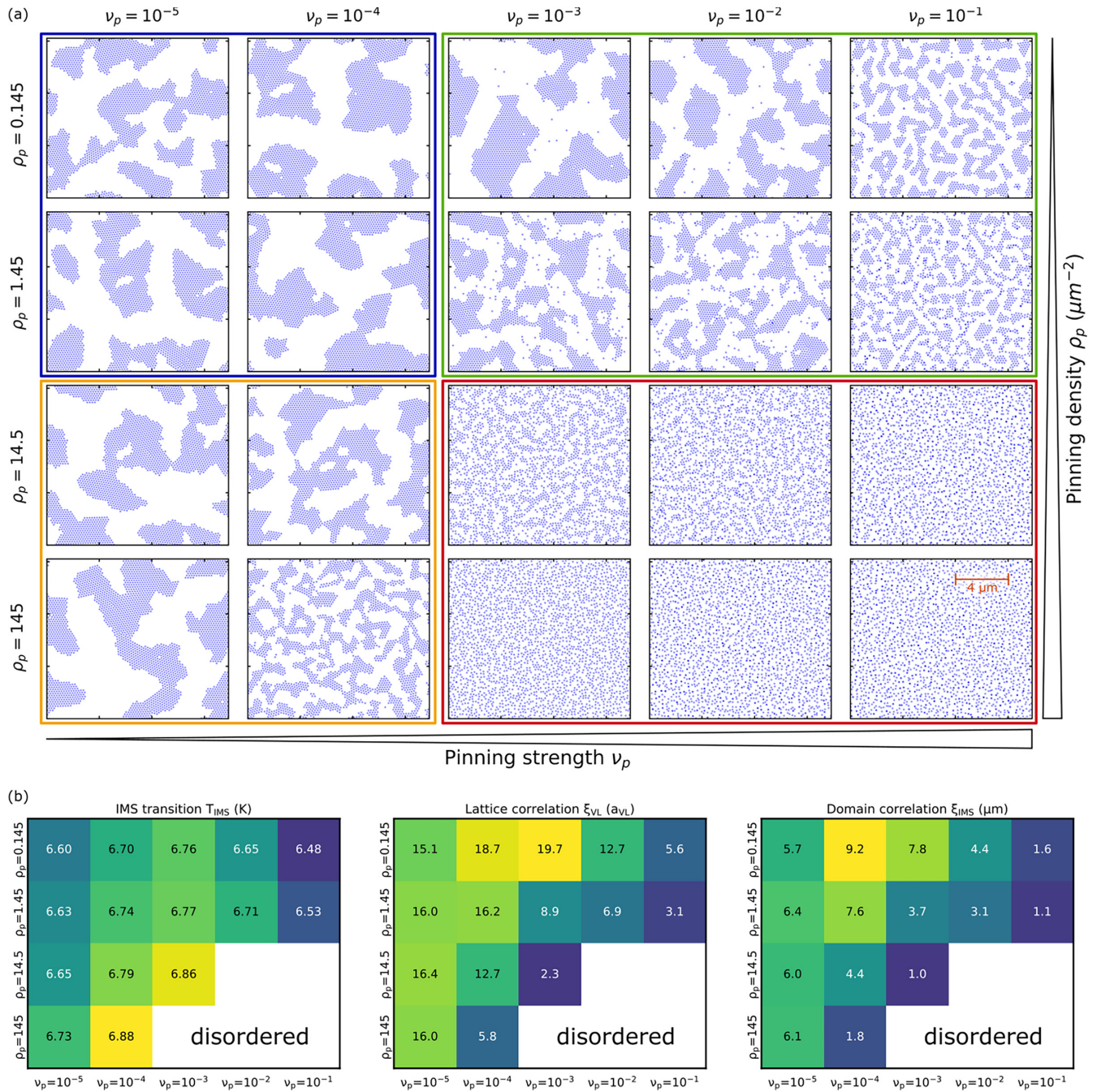


FIG. 4. (a) Real space configurations of all simulations with different  $\rho_p$  and  $\nu_p$  at  $T_{\text{final}} = 6.1$  K. Increasing either parameter decreases the resulting domain size. In the bottom right corner, pinning suppresses both the VL structure and the IMS domain formation. The colored frames indicate different pinning regimes: no pinning (blue), dominant pinning (red), individual pinning (green), collective pinning (orange). (b) Numerical results for  $\xi_{\text{IMS}}$ ,  $\xi_{\text{VL}}$ , and  $T_{\text{IMS}}$ . The two correlation lengths are obviously correlated. The numerical values are highlighted with a corresponding linear color scale for easier visual interpretation.

### B. Influence of pinning

The main part of our paper is to investigate the properties of the IMS under the influence of pinning and in different magnetic fields. The relevant simulation parameters are the density  $\rho_p$  and the strength  $\nu_p$  of the pinning centers, and the flux density  $B_{\text{sim}}$ . We will first address the effects of the pinning strength and the pinning density for a fixed magnetic field. In the second part, we will study the field dependence for three distinct pinning cases. Simulations were

performed for all combinations of the pinning density  $\rho_p = 0.145, 1.45, 14.5, 145.0$  ( $1/\mu\text{m}^2$ ) and the pinning strength  $\nu_p = 10^{-5}, 10^{-4}, 10^{-3}, 10^{-2}, 10^{-1}$ . All further simulation parameters are listed in Table II. Figure 4(a) shows the final vortex configurations at  $T_{\text{fin}}$ . The pinning sites have been omitted in the images for graphical reasons. Darker vortex positions indicate the occupation of multiple vortices. With  $B_{\text{sim}} = 30$  mT, the values of  $\rho_p$  correspond to ratios of  $N_p/N_v = 0.01, 0.1, 1, 10$ . Depending on the parameter



values, three primary regimes can be identified. For large  $\rho_p$  and  $\nu_p$ , the vortex matter is disordered, showing neither a vortex lattice, nor a domain structure. In the opposing case of low  $\rho_p$  and  $\nu_p$ , the system is effectively pinning-free and exhibits a large scale domain structure. In the region between, which is approximately defined by values of  $10^{-4} < \rho_p \cdot \nu_p < 10^{-1}$ , the domain size decreases with increasing pinning parameters. For small  $\rho_p = 0.145, 1.45$  ( $1/\mu\text{m}^2$ ), isolated vortices can be present between the larger VL domains, which are situated on top of pinning centers in all cases.

Numerical values for  $\xi_{\text{IMS}}$  and  $\xi_{\text{VL}}$  at  $T_{\text{fin}}$  and for  $T_{\text{IMS}}$  are shown in Fig. 4(b). Simulations resulting in a disordered state are left blank in the parameter maps.  $\xi_{\text{IMS}}$  and  $\xi_{\text{VL}}$  are clearly correlated: Both length scales have a maximum at  $\rho_p \approx 0.145$  and  $\nu_p \approx 10^{-4}$  and decrease towards larger pinning parameters. The vortex lattice parameter  $a_{\text{VL}}$  is much less affected and lies in the range between  $r_{\text{min}}^{\text{VV}} = 198.0$  nm and  $r_{\text{min}}^{\text{VL}} = 185.2$  nm, except for two simulations at the border to the disordered regime. The transition temperature  $T_{\text{IMS}}$  increases with the pinning strength  $\nu_p$  and has a maximum for  $\rho_p \approx 10^{-3}$ . There is no obvious correlation to the domain size. Compared to the theoretical value of  $T_{\text{IMS}}^{\text{theo}} = 6.92$  K, the undercooling varies considerably between 0.04 K and 0.44 K.

Pinning primarily affects the IMS in two ways: Above the IMS, pinning centers introduce defects and disorder into the vortex lattice, which creates different starting points for the IMS transition. Additionally, the pinning interactions restrict the vortex rearrangement in the IMS. Below, the hallmarks of four major pinning cases are described, with approximate ranges for the pinning parameters.

*No pinning* ( $\rho_p = 0.145, 1.45$ ;  $\nu_p = 10^{-5} - 10^{-5}$ ). In the case of few, weak pinning centers, pinning has no effect on the simulation. The transition into the IMS is well defined by a sharp drop of the lattice parameter  $a_{\text{VL}}$ . The emerging domain morphology depends on the simulation procedure, defined by  $\Delta T$ ,  $S_{\text{T}}$ , and  $\gamma$ , and the inherent undercooling effect.

*Dominant pinning* ( $\rho_p = 14.5, 145$ ;  $\nu_p = 10^{-1} - 10^{-3}$ ). Here the vortex matter is defined by the pinning interactions, rather than the vortex interaction. The initial vortex lattice quickly changes to a random, evenly distributed vortex configuration, which is governed by the pinning positions. A temperature dependence of the vortex configuration is almost completely absent. Depending on the pinning strength, multiple vortices may be trapped at a single pinning site.

*Individual pinning* ( $\rho_p = 0.145, 1.45$ ;  $\nu_p = 10^{-2}, 10^{-3}$ ). Here, the pinning sites are usually isolated, but strong enough to trap a single vortex throughout the whole simulation. This creates local defects in the VL, while the overall lattice coherence remains unaffected. The lattice defects provide initial breaking points and facilitate the IMS transition, which results in an increased  $T_{\text{IMS}}$ . Individual vortices trapped at a pinning site may remain in the Meissner spaces between larger VL domains.

*Collective pinning* ( $\rho_p = 14.5, 145$ ;  $\nu_p = 10^{-5} - 10^{-4}$ ). In this case, VL patches adapt to the underlying pinning structure collectively, which introduces a mosaicity to the lattice. The boundaries and defects between crystallites are preferred breaking points in the IMS transition. Again, this increases  $T_{\text{IMS}}$ . In contrast to individual pinning, the pinning sites also reduce the vortex mobility after the initial break-up.

TABLE II. List of parameters used for the systematic study of  $N_v$  and  $\nu_p$ .

$N_v$	$B_{\text{sim}}$ (mT)	$T_{\text{init}}$ (K)	$T_{\text{final}}$ (K)	$\Delta T$ (K)	$\gamma$	$S_{\text{T}}$	$S_{\text{tot}}$
2450	30	6.9	6.1	0.01	4	25	2025

Therefore, the transition is typically broadened over a larger temperature range.

### C. Field dependence

In this section, we explore the dependence of the IMS on the magnetic flux density  $B_{\text{sim}}$ . As shown in Fig. 1(b), the initial vortex density  $\rho_v$  and the expected transition temperature  $T_{\text{IMS}}^{\text{theo}}$  are field dependent. In contrast, the vortex and pinning interactions as well as the pinning density  $\rho_n$  are independent of the magnetic field.

We present three distinct pinning cases: no pinning (NP) ( $\rho_p = 0, \nu_p = 0$ ), individual pinning (IP) ( $\rho_p = 0.145/\mu\text{m}^2, \nu_p = 10^{-2}$ ), and collective pinning (CP) ( $\rho_p = 14.5/\mu\text{m}^2, \nu_p = 10^{-4}$ ). In the IP case,  $\rho_p$  is small enough to ensure isolated pinning centers.  $\nu_p$  is large enough that the pinning interaction is dominant while still avoiding the pinning of multiple vortices. For CP, the density of pinning sites and vortices is of the same order of magnitude. The pinning interaction is weaker than, but comparable to the vortex interaction. In both cases, we kept a constant value of the product  $\rho_p \cdot \nu_p$ , to achieve a comparable total pinning effect. The magnetic flux density is chosen in the range of  $B_{\text{sim}} = 10, 15, 20, 25, 30, 35, 40$  mT. The remaining simulation parameters are given in Table III.

Results of the final vortex configuration at  $T_{\text{fin}}$  for all fields and pinning cases are shown in Fig. 5(a). Since the number of vortices is fixed, the simulation cell has a different size for each  $B_{\text{sim}}$ . For better comparability, an area of  $10 \times 10 \mu\text{m}^2$  is marked in each panel (orange square). Pinning sites have been omitted in the images. Results at high fields are similar in all pinning cases, demonstrating large labyrinth like morphologies. In contrast, the IMS strongly depends on the pinning case at lower fields, with a tendency towards isolated VL domains. Especially for the IP case, a small number of isolated (pinned) vortices is present in addition. When pinning is absent, the large domains make the changing area fraction of VL domains well visible. This is due to the field dependence of the initial lattice parameter, as opposed to the field independent  $a_{\text{VL}}$  in the IMS, which leads to a different contraction factor of the vortex lattice at  $T_{\text{fin}}$ .

TABLE III. List of parameters used for the systematic study of  $B_{\text{sim}}$  for three distinct pinning cases.

$N_v$	$T_{\text{init}}$ (K)	$T_{\text{final}}$ (K)	$\Delta T$ (K)	$\gamma$	$S_{\text{T}}$	$S_{\text{tot}}$		
2450	7.5	6.1	0.01	4	25	3425		
	$B_{\text{sim}}$	10 mT	15 mT	20 mT	25 mT	30 mT	35 mT	40 mT
NP	$N_p$							
IP	$N_p$	74	49	37	29	25	21	18
CP	$N_p$	7350	4900	3675	2940	2450	2100	1838

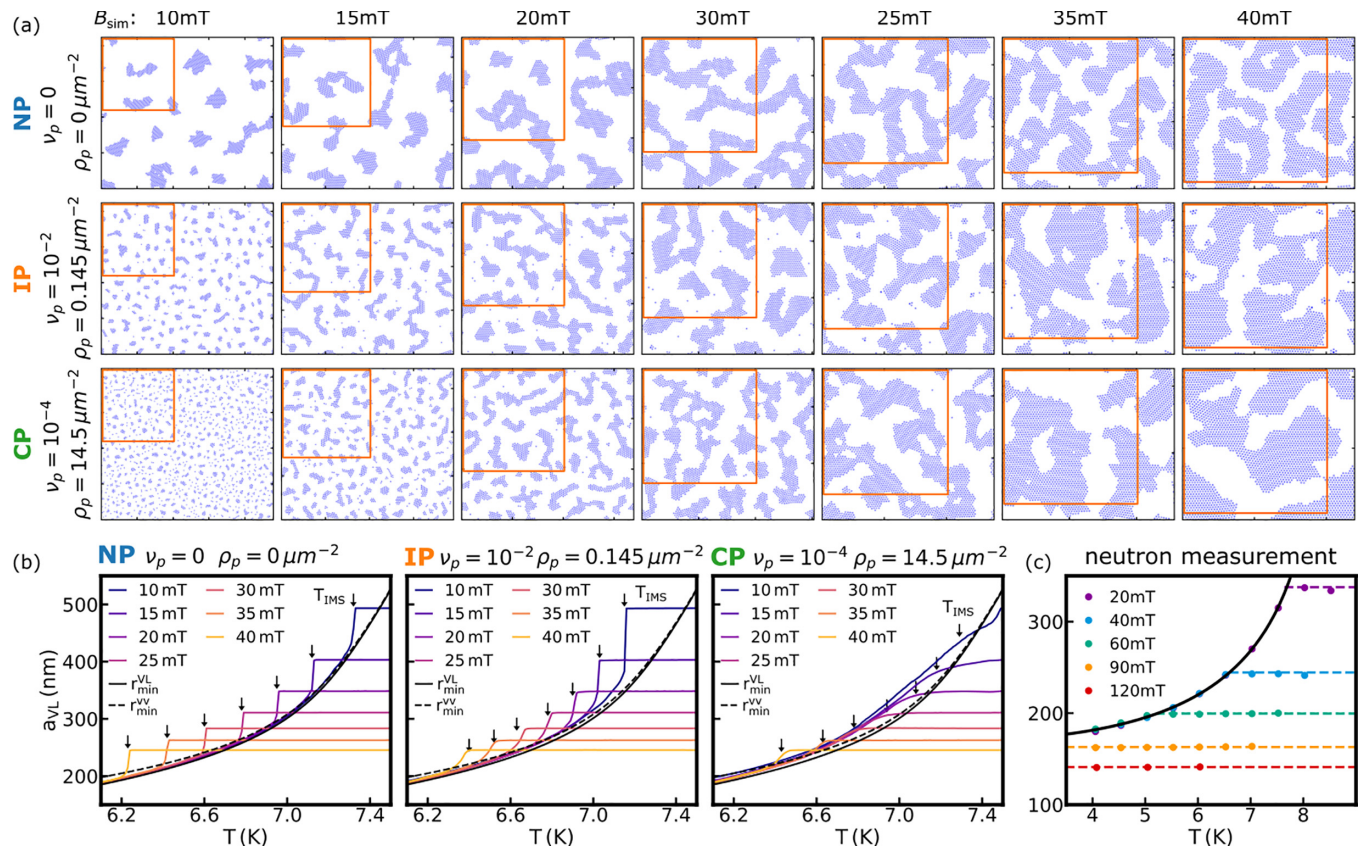


FIG. 5. (a) Real space vortex configurations at  $T_{fin}$  in different fields  $B_{sim}$  for the pinning cases: NP, IP, and CP. The orange rectangles have the same size of  $10 \mu\text{m}$  in all images. (b) Temperature dependence of the VL parameter  $a_{VL}$ . The IMS transition temperatures are marked by small arrows. (c) Measured lattice parameter of a niobium single crystal. Panel (c) was taken with permission from [29].

Figure 5(b) shows the vortex lattice parameter  $a_{VL}$  of all simulations including the predicted values for the preferred vortex separation,  $r_{min}^{VL}$  and  $r_{min}^{VV}$ . Note that the EGL results do not depend on the pinning. In the NP and IP cases,  $a_{VL}$  behaves very similarly and as seen in the example in Fig. 3(b). The IMS transition temperature  $T_{IMS}$  is field dependent and defined by a sharp drop of  $a_{VL}$ . In the IP case, the transition is broadened at high fields and slight deviations from the theory line are present at higher temperatures. Additionally,  $T_{IMS}$  and the undercooling is different in both cases. In contrast, collective pinning (CP) shows a smooth change of the lattice parameter, especially at low fields. Due to the absence of a clear feature, instead of  $a_{VL}$ , the real space images of the simulation steps were used to determine  $T_{IMS}$ . At the onset of the IMS transition, gaps in the homogeneous vortex lattice start to form, which are well visible but do not immediately affect the mean lattice parameter. In the IMS,  $a_{VL}(T)$  is very slightly depending on the magnetic field. In contrast to the other pinning cases, the values deviate strongly from  $r_{min}^{VL, VV}(T)$ . Note, that the simulation at 10 mT contains a very large number of individually pinned vortices and is close to a disordered state.

For comparison, Fig. 5(c) shows experimental data obtained via small angle neutron scattering on a niobium single crystal exhibiting nearly perfect macroscopic flux trapping [29]. The two distinct regions of  $a_{VL}$  in the Shubnikov state and in the IMS are clearly visible. An undercooling can not be observed, as all data points in the IMS lie perfectly on a single curve. Considering the low number of data points, the

neutron measurements most closely resemble the CP simulation results.

The field dependence of  $T_{IMS}$  is shown in Fig. 6(a), including the theoretical prediction  $T_{IMS}^{theo}$ . The associated undercooling  $\delta T_{uc} = T_{IMS}^{VL} - T_{IMS}^{theo}$  is plotted in Fig. 6(b). Both  $T_{IMS}^{theo}$  and  $\delta T_{uc}$  change by a similar amount with  $B_{sim}$ . Note, that  $T_{IMS}$  and  $\delta T_{uc}$  have no clear hierarchy for the pinning cases, but order is reversed at  $B_{sim} \approx 25$  mT.

Figures 6(c) and 6(d) show the correlation lengths  $\xi_{VL}$  and  $\xi_{IMS}$  at  $T_{fin}$ . In the cases IP and CP, both quantities have a similar field dependence and increase with  $B_{sim}$ . The deviation from a linear trend above  $\approx 30$  mT is presumably connected to the limitations of the simulation cell size. Without pinning (NP)  $\xi_{IMS}$  decreases with increasing field, while  $\xi_{VL}$  is field independent. Figure 6(e) shows results for  $\xi_{IMS}$  obtained experimentally using ultra small angle neutron scattering measurements [28]. The sample was a lower quality niobium single crystal exhibiting nearly perfect macroscopic flux trapping. Similar to the pinning cases IP and CP, the domain size increases with the applied magnetic field.

The field dependence of the correlation lengths shows a clearly different behavior for the cases with and without pinning. For the NP case, we find a field independent VL-domain size  $\xi_{VL}$ , which is presumably defined by the field cooling procedure. The increasing domain size in both pinning cases shows that the morphology is dictated not only by the field independent density of pinning centers. The differences in the transition temperature and the undercooling depend on a



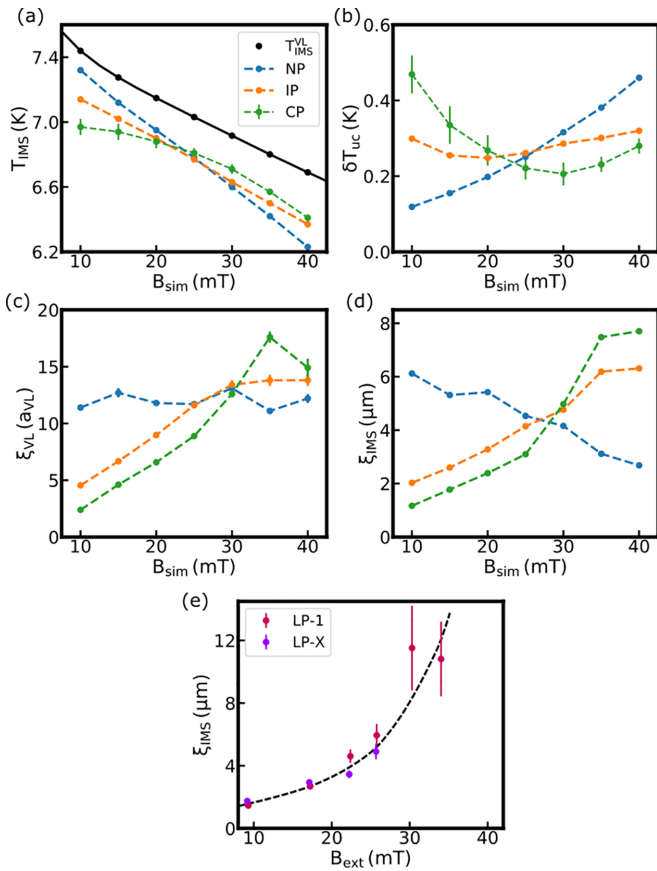


FIG. 6. (a) Field dependence of the IMS transition temperature  $T_{\text{IMS}}$ . Included is the theoretically expected transition temperature  $T_{\text{IMS}}^{\text{VL}}$ . (b) Undercooling temperature  $\delta T_{\text{uc}}$ . All three pinning cases show distinct behaviors, including a reversal at  $B_{\text{sim}} \approx 25$  mT. [(c),(d)] Temperature dependence of the correlation lengths  $\xi_{\text{VL}}$  and  $\xi_{\text{IMS}}$ . The cases IP and CP can be easily distinguished from the pinning free case NP. (e) Measured  $\xi_{\text{IMS}}$  of a niobium single crystal. The data shown in (e) was taken with permission from [28].

large variety of factors, like the relative density of vortices and pinning centers, the relative strength of vortex and pinning interactions, thermal fluctuations, as well as the rate of change of  $r_{\text{min}}^{\text{VV}}$  contribute to the vortex configuration. Therefore, a precise determination of the origin of these different behaviours was outside the scope of this study.

#### IV. SUMMARY

We have presented two-dimensional molecular dynamics simulations of the vortex matter in the intertype (IT) superconducting regime, in an attempt to understand and describe recent results on niobium. In the calculations, we used results derived in the extended Ginzburg-Landau formalism to model the nonmonotonic interaction responsible for the formation of the intermediate mixed state (IMS). Within the framework of the molecular dynamics formalism, we studied the dependence of the IMS vortex matter on vortex pinning and the magnetic field, in a field cooling procedure where the global vortex density is kept constant, emulating a perfect macroscopic flux trapping scenario.

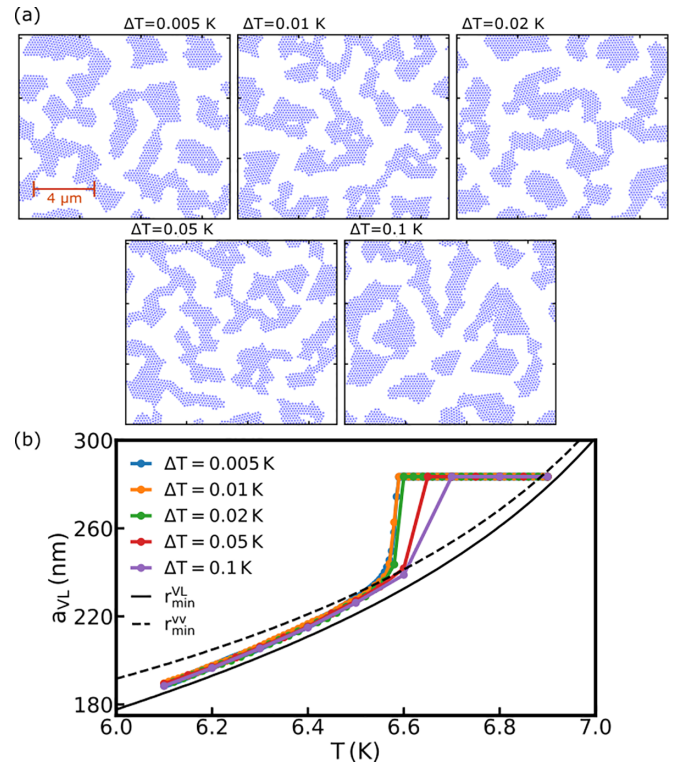


FIG. 7. (a) Real space images of the vortex configuration at  $T_{\text{final}} = 6.1$  K. Apparently, the variation of  $\Delta T$  has no effect on the simulations. (b) Temperature dependence of the VL-parameter  $a_{\text{VL}}(T)$ . The initial VL is significantly cooled below the expected transition temperature of 6.92 K.

The IMS transition is observed as the fracturing of a homogeneous vortex lattice into a domain structure. Hallmarks of the IMS are a decreasing lattice parameter  $a_{\text{VL}}$  while lowering the temperature, a reduced lattice coherence length  $\xi_{\text{VL}}$ , and a characteristic length scale of the domain morphology  $\xi_{\text{IMS}}$ .  $a_{\text{VL}}$  is closely related to the position  $r_{\text{min}}^{\text{VV,VL}}(T)$  of a minimum in the interaction potential. The main result of our simulations is the exceptional stability of the IMS transition, which emerged over orders of magnitude of the pinning density  $\rho_{\text{p}}$  and the pinning strength  $v_{\text{p}}$ , and which can be confirmed by experiments on niobium samples of distinctly varying quality [29]. Only if the pinning is strong enough to result in a strongly disordered vortex lattice, the IMS transition was not observed.

In pinning free simulations, the IMS properties showed a strong dependence on the cooling procedure, which amounts to a dependence on the chosen relaxation time. Without further influences, the long-range vortex attraction drives a vortex system towards merging into a single large domain, which is unphysical. When the relaxation time increases, we expect a scenario similar to the intermediate state in type-I superconductors, where demagnetization effects and dipolar magnetic interactions lead to a large-scale domain structure [52]. The cooling procedure revealed a prominent undercooling of the vortex system below the theoretically predicted transition temperature. This is only weakly affected by details of the cooling procedure but changed notably with the pinning conditions and the magnetic field. We attribute this undercooling

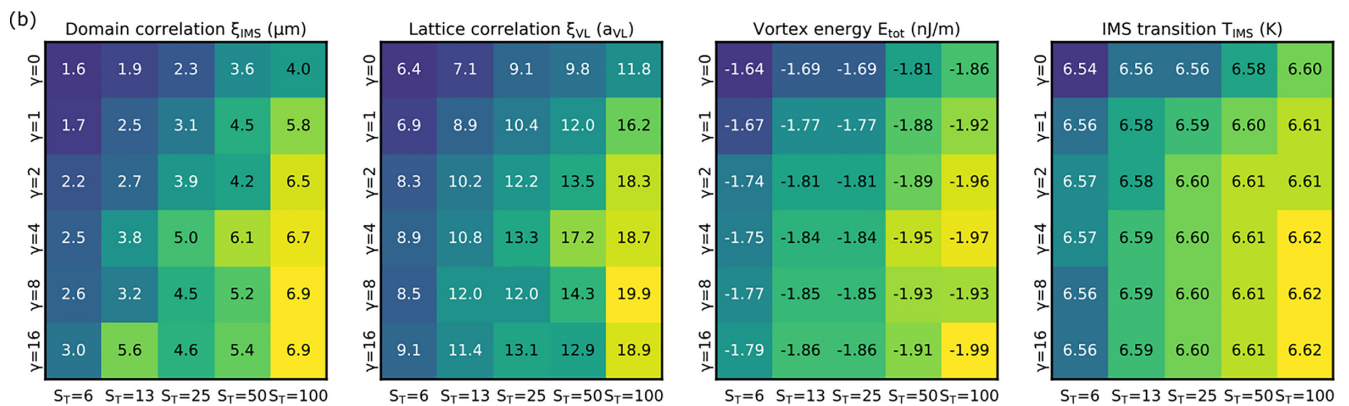
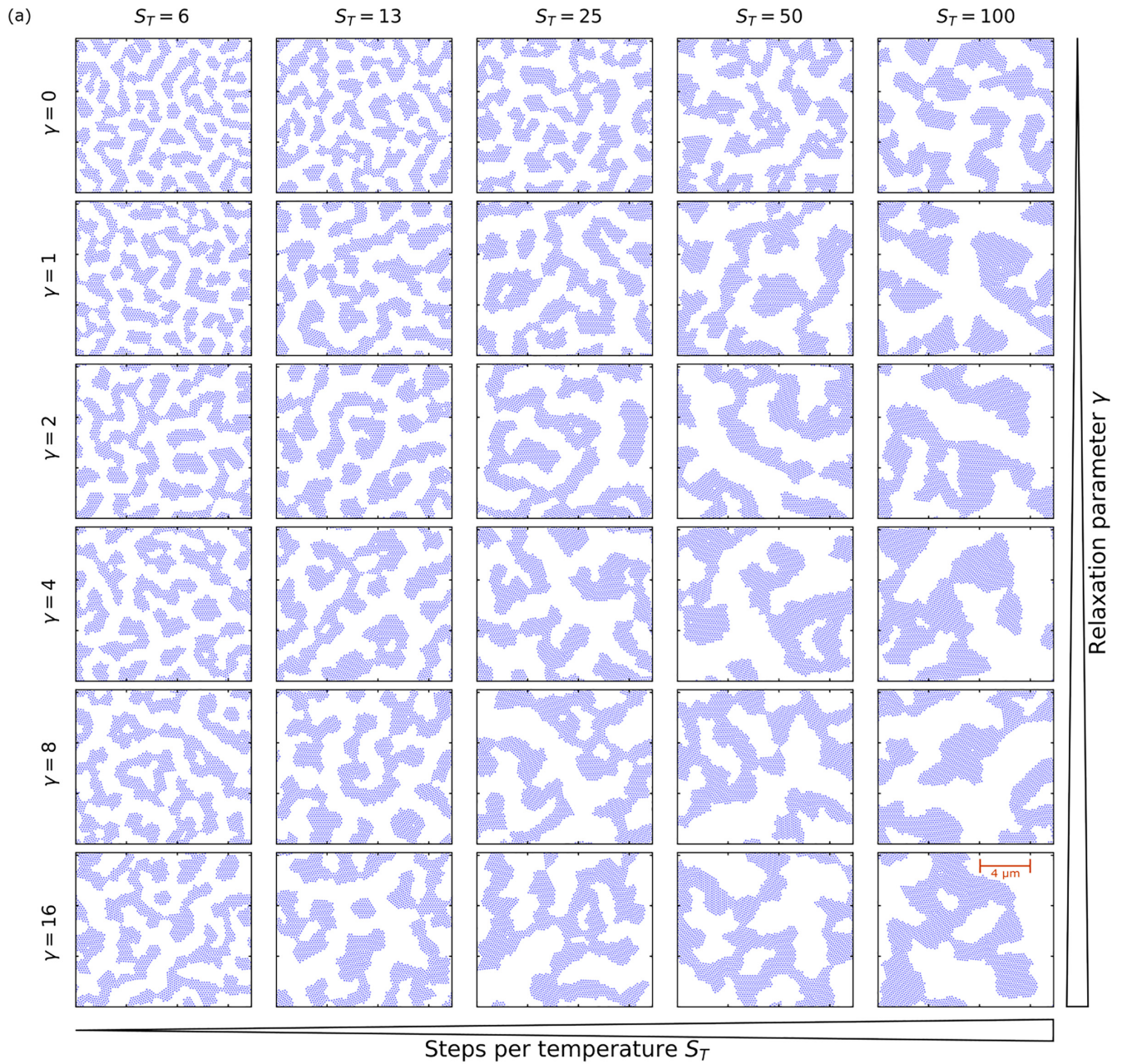


FIG. 8. (a) Real space configurations of all simulations with different  $S_T$  and  $\gamma$  at  $T_{\text{final}} = 6.1$  K. Increasing either parameter increases the resulting domain size. (b) numerical results for  $\xi_{\text{IMS}}$ ,  $\xi_{\text{VL}}$ ,  $E_{\text{tot}}$  and  $T_{\text{IMS}}$ . All parameters show similar systematics with respect to both varied parameters. The numerical values are highlighted with a corresponding linear color scale for easier visual interpretation.



in primarily to the perfect initial lattice arrangement and suggest further studies with different initial vortex configurations are needed to clarify details of this transition.

Pinning has a measurable effect on the IMS over a large parameter space defined approximately by  $10^{-1} > \rho_p \cdot v_p > 10^{-4}$  and spanning at least four orders of magnitude in both individual parameters. The most visible effect of pinning is to reduce the IMS domain size at larger  $\rho_p \cdot v_p$ . The detailed impact of pinning on the vortex matter depends mainly on two effects: Creating defects in the VL in the Shubnikov state and reducing the vortex mobility of isolated vortices and the lattice as a whole, alike. Qualitatively, the main differences between different pinning cases (such as IP and CP) are visible in the lattice parameter, which undergoes a sharp drop at the IMS transition for individual pinning and a broad and smooth change for collective pinning. The emerging domain morphology defined by  $\xi_{VL}$  and  $\xi_{IMS}$  is, however, very similar. Simulations with and without pinning yield visibly discernible result for the field dependence of both parameters. In contrast, the cases with pinning, IP and CP, are qualitatively very similar and only show small quantitative differences.

The undercooling observed in most simulations prompts the occurrence of hysteretic effects in the vortex matter between cooling and heating procedures especially in pinning free cases, heating up from the IMS into the Shubnikov phase, it is unreasonable to expect a perfect VL to re-form, as was the starting point of our simulations. It is likely for the vortex matter to follow the theoretical  $a_{VL}$  line closely up to the transition temperature and end up as a somewhat imperfect VL. Since pinning introduces an initial disorder before cooling down, we expect a similar configuration to reemerge after subsequently warming up. However, more pronounced differences in the  $a_{VL}(T)$  dependence might occur due to the interaction of pinning landscape and the vortices or collective IMS domains. In our neutron experiments, we were unable to observe hysteresis between cooling and heating, which might be used in further studies to distinguish the pinning configuration representing the real sample. Based on magnetization measurements and neutron grating interferometry, we know that cycling the magnetic field leads to strong hysteretic effects. These are, however, largely due to the macroscopic sample geometry and its impact on flux entering and leaving the sample. The occurring effect is well described in the critical state model and amounts to a macroscopically inhomogeneous flux distribution in the sample, which can even lead to the coexistence of IMS and Shubnikov state. In our simulations, these effects are challenging to incorporate, since they require a changing number of vortices and happen at a much larger length scale.

In contrast to previous studies, we were unable to reproduce an IMS state with a well-ordered, periodic domain superstructure. We attribute this mainly to the long-range behavior of the chosen vortex interaction, which is attractive in this paper instead of the repulsion typically associated with type-II superconductivity. The formation of superstructures might be associated with an additional long-range repulsion, e.g., due to stray fields. An additional influence from finite size effects of the simulations can also not be ruled out, since the number of domains in most MD simulations is quite limited. We also note that the results presented here use only

a singular value of the Ginzburg-Landau parameter  $\kappa$ . This fixes the relative strength of the attractive and repulsive components in the vortex interaction and might thereby prohibit the formation of a superstructure.

Results from theoretical simulation and experiments of the IMS transition in pure niobium have demonstrated a very good agreement. The agreement is especially good in the temperature dependence of the vortex lattice parameter and the field and temperature dependence of the IMS domain morphology indicated by the correlation lengths  $\xi_{VL}$  and  $\xi_{IMS}$ . The experimental data is best represented by the collective pinning case. However, this result might be distorted by the more obvious undercooling effect of the individual pinning simulations. For a comprehensive comparison of simulations and experiments, we propose a further refinement for the cooling procedure in the simulations and additional experimental results of samples with well-defined pinning properties.

The motivation for the presented simulations lies primarily in recreating the conditions of our past neutron experiments and aid us in understanding the microscopic properties of the vortex matter not accessible by those techniques. However, such simulations are easily expanded on. One possible study would be to address the above mentioned hysteretic effects, by extending the rather simple cooling procedure by arbitrary temperature cycles. A different route, which has been taken in several similar studies is to examine the effect of specially structured arrangements of pinning centers. This approach, in many cases, found the emergence of new superstructures in the vortex matter, such as line patterns or hexagonal domain arrangements [53,54]. Additional cases, such as field changes, might be more challenging to implement correctly. Due to demagnetization effects or geometric barriers and the limited mobility of vortices in the sample, a macroscopically inhomogeneous flux distribution may occur, described well in the critical state model [55]. The effects of a driving current have been a further topic in previous papers [32,56]; however, the very inhomogeneous superconducting state in the IMS make such studies with molecular dynamics simulations challenging since the current density distribution is closely coupled to the vortex domain structure [38]. It remains, as a closing remark, that the combination of simulations and experiments poses a powerful tool in understanding the physics behind a complex system.

## ACKNOWLEDGMENTS

We would like to express our gratitude to Sebastian Busch for valuable input on the method of molecular dynamics simulations and to Michael Schulz and Arkady Shanenko for fruitful discussions on the topic of the formation of the

TABLE IV. List of parameters used in the systematic study of  $\Delta T$  (c.f. Fig. 7).

$N_v$	$N_p$	$B_{sim}$ (mT)	$T_{init}$ (K)	$T_{final}$ (K)	$\gamma$	$S_T / \Delta T$
2450	–	30	6.9	6.1	0	5000
	$\Delta T$ (K)	0.005	0.01	0.02	0.05	0.1
	$S_T$	25	50	100	250	500

TABLE V. Results of the simulation analysis.  $\xi_{\text{IMS}}$ ,  $\xi_{\text{VL}}$ , and  $a_{\text{VL}}$  are the values at  $T_{\text{fin}}$ . None of the results indicate a significant dependence of the IMS transition on the temperature step size  $\Delta T$ .

$\Delta T$ (K)	0.005	0.01	0.02	0.05	0.1
$T_{\text{IMS}}$ (K)	6.585(5)	6.58(1)	6.58(2)	6.60(5)	6.6(1)
$\xi_{\text{IMS}}$ ( $\mu\text{m}$ )	3.3(3)	3.6(3)	3.5(3)	3.2(3)	3.0(3)
$\xi_{\text{VL}}$ ( $a_{\text{VL}}$ )	5.8(1)	4.9(1)	5.5(1)	5.1(1)	5.4(1)
$a_{\text{VL}}$ (nm)	188.96	189.60	188.55	189.36	188.41

intermediate mixed state (IMS) in intertype superconductors. A.V. acknowledges support from CAPES (Brazil) within the framework of the PRINT program Edital No. 41/2017, and from the SUPERLAB at the UFPE University (Brazil).

#### APPENDIX A: TIME STEPS

The flexible duration of the time steps  $\Delta t$  is governed by an upper and lower limit of the maximum vortex displacement  $r_{\text{max}}$  occurring in any simulation step. The maximum value is set to be 10% of the separation expected for neighboring vortices. This is given by the field dependent vortex lattice parameter in the Shubnikov state and by the vortex interaction potential minimum  $r_{\text{VV}}^{\text{min}}$  in the IMS (c.f. the discussion of  $F_{\text{VV}}$  in Sec. I.3.). A stagnation of the simulations is prevented by choosing a lower boundary, which is set to be 10% of  $r_{\text{max}}$ . Each time one of these thresholds is crossed,  $\Delta t$  is changed to a new value to prevent this from happening.

#### APPENDIX B: PINNING FREE SIMULATIONS

This Appendix contains detailed parameters and results of the pinning free simulations discussed in Sec. III A.

TABLE VI. List of parameters used in the systematic study of  $\gamma$  and  $S_{\text{T}}$  (c.f. Fig. 8).

$N_{\text{v}}$	$N_{\text{p}}$	$B_{\text{sim}}$ (mT)	$T_{\text{init}}$ (K)	$T_{\text{final}}$ (K)	$\Delta T$ (K)
2450	–	30	6.9	6.1	0.01 (K)

For the study addressing the temperature steps  $\Delta T$ , Table IV shows the simulation parameters. Figure 7(a) shows results for the final vortex configurations for  $\Delta T = 0.005, 0.01, 0.02, 0.05, 0.1$  K. The impact of this parameter is visually indistinguishable. Figure 7(b) shows the evolution of the lattice parameter  $a_{\text{VL}}$  with temperature, which is almost identical, except for the different number of data points. Table V contains corresponding numerical results for the transition temperature  $T_{\text{IMS}}$  and the vortex matter properties  $\xi_{\text{IMS}}$ ,  $\xi_{\text{VL}}$ , and  $a_{\text{VL}}$ , evaluated at  $T_{\text{fin}} = 6.1$  K. Similarly, the simulation parameters for the study of  $\gamma$  and  $S_{\text{T}}$  are given in Table VI, where  $\gamma = 0, 1, 2, 4, 8, 16$  and  $S_{\text{T}} = 6, 13, 25, 50, 100$  are used. The results are summarized in Fig. 8, where panel (a) shows the final vortex configurations at  $T_{\text{fin}}$  and panel (b) contains numerical results for  $\xi_{\text{VL}}$ ,  $\xi_{\text{IMS}}$ ,  $T_{\text{IMS}}$ , and the total vortex interaction energy  $E_{\text{tot}}$ . A trend towards larger domain sizes with increasing  $\gamma$  and  $S_{\text{T}}$  is clearly visible in panel (a) and confirmed by the numerical results. The transition into the IMS, as signified by the temperature evolution of  $a_{\text{VL}}$  (not shown), is not affected qualitatively by either of the considered parameters. The same is true for the topology of the IMS, which always shows a random interconnected labyrinth of the vortex free Meissner state.

- [1] R. P. Hübner, *Magnetic Flux Structures of Superconductors*, 2nd ed. (Springer-Verlag, Berlin, 2001).
- [2] E. H. Brandt, *Rep. Prog. Phys.* **58**, 1465 (1995).
- [3] E. Brandt and U. Essmann, *Phys. Stat. Solidi B* **144**, 13 (1987).
- [4] U. Klein, *J. Low Temp. Phys.* **69**, 1 (1987).
- [5] N. Sluchanko, S. Gavrilkin, K. Mitsen, A. Kuznetsov, I. Sannikov, V. Glushkov, S. Demishev, A. Azarevich, A. Bogach, A. Lyashenko *et al.*, *J. Supercond. Nov. Magn.* **26**, 1663 (2013).
- [6] J. Y. Ge, J. Gutierrez, A. Lyashchenko, V. Filipov, J. Li, and V. V. Moshchalkov, *Phys. Rev. B* **90**, 184511 (2014).
- [7] P. K. Biswas, A. D. Hillier, R. P. Singh, N. Parzyk, G. Balakrishnan, M. R. Lees, C. D. Dewhurst, E. Morenzoni, and D. M. Paul, *Phys. Rev. B* **102**, 144523 (2020).
- [8] V. Moshchalkov, M. Menghini, T. Nishio, Q. H. Chen, A. V. Silhanek, V. H. Dao, L. F. Chibotaru, N. D. Zhigadlo, and J. Karpinski, *Phys. Rev. Lett.* **102**, 117001 (2009).
- [9] E. H. Brandt and M. P. Das, *J. Supercond. Nov. Magn.* **24**, 57 (2011).
- [10] E. Babaev and M. Speight, *Phys. Rev. B* **72**, 180502(R) (2005).
- [11] J. Gutierrez, B. Raes, A. V. Silhanek, L. J. Li, N. D. Zhigadlo, J. Karpinski, J. Tempere, and V. V. Moshchalkov, *Phys. Rev. B* **85**, 094511 (2012).
- [12] E. Babaev, J. Carlström, M. Silaev, and M. Speight, *Type-1.5 Superconductivity: From Basic Research to Applications, in Superconductors at the Nanoscale* (De Gruyter, Boston, 2017).
- [13] V. A. Berezin and V. A. Tulin, *Phys. Solid State* **42**, 415 (2000).
- [14] A. Buzdin and I. Baladie, *Phys. Rev. Lett.* **88**, 147002 (2002).
- [15] A. V. Samokhvalov, A. S. Mel'nikov, and A. I. Buzdin, *Phys. Rev. B* **85**, 184509 (2012).
- [16] V. O. Dolocan, C. Veauvy, F. Servant, P. Lejay, K. Hasselbach, Y. Liu, and D. Mailly, *Phys. Rev. Lett.* **95**, 097004 (2005).
- [17] A. Vagov, A. A. Shanenko, M. V. Milošević, V. M. Axt, V. M. Vinokur, J. A. Aguiar, and F. M. Peeters, *Phys. Rev. B* **93**, 174503 (2016).
- [18] A. Vagov, S. Wolf, M. D. Croitoru, and A. A. Shanenko, *Commun. Phys.* **3**, 58 (2020).
- [19] S. Wolf, A. Vagov, A. A. Shanenko, V. M. Axt, and J. A. Aguiar, *Phys. Rev. B* **96**, 144515 (2017).
- [20] R. M. Da Silva, M. V. Milošević, A. A. Shanenko, F. M. Peeters, and J. A. Aguiar, *Sci. Rep.* **5**, 12695 (2015).
- [21] E. Babaev, J. Carlström, and M. Speight, *Phys. Rev. Lett.* **105**, 067003 (2010).
- [22] F. N. Rybakov and E. Babaev, *J. Math. Phys.* **62**, 121901 (2021).
- [23] R. Wiesendanger, *Rev. Mod. Phys.* **81**, 1495 (2009).
- [24] M. R. Koblischka and U. Hartmann, *Ultramicroscopy* **97**, 103 (2003).
- [25] A. Hubert and R. Schäfer, *Magnetic Domains* (Springer, Berlin, 1998).
- [26] S. Mühlbauer, D. Honecker, É. A. Périgo, F. Bergner, S. Disch, A. Heinemann, S. Erokhin, D. Berkov, C. Leighton, M. R. Eskildsen *et al.*, *Rev. Mod. Phys.* **91**, 015004 (2019).



- [27] T. Reimann, S. Mühlbauer, M. Schulz, B. Betz, A. Kaestner, V. Pipich, P. Böni, and C. Grünzweig, *Nat. Commun.* **6**, 8813 (2015).
- [28] T. Reimann, M. Schulz, D. F. R. Mildner, M. Bleuel, A. Brület, R. P. Harti, G. Benka, A. Bauer, P. Böni, and S. Mühlbauer, *Phys. Rev. B* **96**, 144506 (2017).
- [29] A. Backs, M. Schulz, V. Pipich, M. Kleinhan, P. Böni, and S. Mühlbauer, *Phys. Rev. B* **100**, 064503 (2019).
- [30] C. J. Olson, C. Reichhardt, and F. Nori, *Phys. Rev. B* **56**, 6175 (1997).
- [31] J. Wang, Z. G. Zhao, M. Liu, D. Y. Xing, and J. M. Dong, *Europhys. Lett.* **65**, 89 (2004).
- [32] Y. Fily, E. Olive, and J. C. Soret, *Phys. Rev. B* **79**, 212504 (2009).
- [33] X. B. Xu, H. Fangohr, S. Y. Ding, F. Zhou, X. N. Xu, Z. H. Wang, M. Gu, D. Q. Shi, and S. X. Dou, *Phys. Rev. B* **83**, 014501 (2011).
- [34] P. Paturi, M. Malmivirta, T. Hynninen, and H. Huhtinen, *J. Phys.: Condens. Matter* **30**, 315902 (2018).
- [35] H. J. Zhao, V. R. Misko, J. Tempere, and F. Nori, *Phys. Rev. B* **95**, 104519 (2017).
- [36] We note that while we are using molecular dynamics simulations, the IMS transition should not be viewed as a dynamic process but rather as a quasi-static relaxation into a new ground state, following changes of the vortex interaction. As such, we will not be evaluating any dynamic properties related to the vortex movement but consider only the properties of static states after each temperature change.
- [37] A. Backs, Vortex matter of the intertype superconductor niobium studied by neutron imaging, neutron diffraction and molecular dynamics simulations, Ph.D. thesis, Technische Universität München, 2021.
- [38] X. S. Brems, S. Mühlbauer, W. Y. Córdoba-Camacho, A. A. Shanenko, A. Vagov, J. A. Aguiar, and R. Cubitt, *Supercond. Sci. Technol.* **35**, 035003 (2022).
- [39] B. Rosenblum and M. Cardona, *Phys. Rev. Lett.* **12**, 657 (1964).
- [40] Y. B. Kim, C. F. Hempstead, and A. R. Strnad, *Phys. Rev.* **139**, A1163 (1965).
- [41] C. J. Olson, C. Reichhardt, and F. Nori, *Phys. Rev. Lett.* **81**, 3757 (1998).
- [42] X. B. Xu, Y. Liu, H. Fangohr, L. Zhang, S. Y. Ding, Z. H. Wang, S. L. Liu, G. J. Wu, and H. M. Shao, *Phys. Rev. B* **73**, 214521 (2006).
- [43] J. Bardeen and M. J. Stephen, *Phys. Rev.* **140**, A1197 (1965).
- [44] H. J. Jensen, A. Brass, A. C. Shi, and A. J. Berlinsky, *Phys. Rev. B* **41**, 6394 (1990).
- [45] E. H. Brandt, *J. Low Temp. Phys.* **53**, 71 (1983).
- [46] A. Brass and H. J. Jensen, *Phys. Rev. B* **39**, 9587 (1989).
- [47] X. B. Xu, H. Fangohr, Z. H. Wang, M. Gu, S. L. Liu, D. Q. Shi, and S. X. Dou, *Phys. Rev. B* **84**, 014515 (2011).
- [48] C. Reichhardt, J. Drocco, C. J. O. Reichhardt, and A. R. Bishop, *Physica C: Superconductivity* **479**, 15 (2012).
- [49] R. Labusch, *Phys. Rev.* **170**, 470 (1968).
- [50] A. Houghton, R. A. Pelcovits, and A. Sudbø, *Phys. Rev. B* **40**, 6763 (1989).
- [51] E. H. Brandt, *Phys. B: Condens. Matter* **169**, 91 (1991).
- [52] J. D. Livingston and W. DeSorbo, in *Superconductivity*, Vol. 2 (Routledge, New York, 1969).
- [53] K. Harada, O. Kamimura, H. Kasai, T. Matsuda, A. Tonomura, and V. V. Moshchalkov, *Science* **274**, 1167 (1996).
- [54] C. Reichhardt, C. J. Olson, and F. Nori, *Phys. Rev. B* **57**, 7937 (1998).
- [55] D. M. Gokhfeld, *Phys. Solid State* **56**, 2380 (2014).
- [56] C. Reichhardt and C. J. Olson Reichhardt, *Rep. Prog. Phys.* **80**, 026501 (2016).